Fragments kinetic energy distribution and half-lives of the true ternary fission for ^{254}Cf isotope in different geometries

M. R. Pahlavani[1,*] and M. Saeidi Babi[1,†]

[1]*Department of Nuclear Physics, Faculty of Basic Science, University of Mazandaran, P.O.Box 47415-416, Babolsar, Iran*

(Dated: December 31, 2024)

Abstract

This study explores the ternary fission of the ^{254}Cf isotope, focusing on various fragmentation in the collinear and the equatorial fragment geometries. The analysis considers the role of magic, double-magic, and even-even fragments in determining the driving potential, the penetration probabilities, the yields, and the decay constants. The results show that the collinear geometry is energetically favored due to lower driving potential, especially when magic or near-magic fragments are involved. Also, the kinetic energy distribution of the fragments are calculated for various combinations. Using the momentum and the energy conservation, the fission Q-value is shared among the fragments in various fragmentation. The results indicate that collinear geometries lead to a more balanced energy distribution, when lighter fragments located at the middle. This agrees well with the observations and provides a clearer picture of the energy dynamics in ternary fission. These findings highlight the influence of the nuclear structure on fragment selection and the energy partitioning, offering new insights into the mechanism for ternary fission of heavy nuclei.

Keywords: true ternary fission; equatorial and collinear geometries; penetration probability; driving potential; half-life; kinetic energy distribution

* m.pahlavani@umz.ac.ir

† m.saeidi04@umail.umz.ac.ir

INTRODUCTION

Undoubtedly, the discovery of fission by Hahn, Meitner, and Strassmann in 1937 [1] has been one of the most significant developments in human life, as by using it, humans were able to extract and use nuclear energy. In nuclear physics, the phenomenon of fission, especially its binary and ternary modes, has occupied the scientific community for decades. Binary fission has been widely studied due to its importance in nuclear energy production. Fission can occur spontaneously or be induced by neutrons, charged particles, and energetic γ-rays [2–10]. Ternary fission presents intriguing possibilities and challenges that require thorough exploration, while it occurs rarely compared to binary fission.

Ternary fission, in which three fragments are released simultaneously, along with binary fission, provides valuable insights into the dynamics and mechanics of nuclear fission. Unlike binary fission, which accounts for the largest number of fission events and has therefore been extensively studied, ternary fission constitutes a much smaller fraction of fission events and has been less studied. Experimental observations also suggest that the probability of the ternary fission is substantially lower than binary fission. For instance, Rosen and Hudson [11] demonstrated that the probability of the ternary fission is approximately 6.7 ± 3 per 10^6 binary fission events in the neutron induced fission of ^{235}U isotope, an interaction that has been widely used to produce nuclear energy.

The spontaneous breakup of a heavy or superheavy nucleus into three fission fragments, referred to as cold ternary fission, is considered a very rare process compared to the spontaneous binary fission. Typically, one of the ternary fission fragments is much lighter than the other two main fragments, leading to the term light-charged-particle-accompanied (LCP-accompanied) ternary fission. In most cases of the LCP-accompanied ternary fission, the LCPis emitted perpendicularly to the heavier fragments due to the Coulomb repulsion because of its formation in the neck region of the scission criteria of the parent nucleus [12, 13], resulting in the equatorial ternary fission. However, in true ternary fission, where the parent nucleus splits into three fragments of comparable masses, all fragments prefer to escape collinearly. True ternary fission primarily occurs in heavy and superheavy nuclei with large fissility parameters ($Z^2/A > 31$), indicating the dominance of Coulomb repulsion over nuclear binding forces [14].

The concept of ternary fission dates back to the early 1940s, initially theorized by San-

Tsiang et al. [15–19]. Subsequent experimental and theoretical investigations, such as those by Titterton [20] and Flynn [21], explored ternary fission processes and their fragment characteristics. Geometrical models for tri-nuclear molecules have been developed since, considering prolately deformed nuclei connected in the line with higher multipole deformations, such as hexadecapole components [22]. These models have been applied to configurations like ^{96}Sr + ^{10}Be + ^{146}Ba, demonstrating the utility of tri-nuclear molecules approach.

Studies on superheavy nuclei have demonstrated the interesting properties of the ternary fission. Calculations by Schulthe is [23] indicates higher relative penetrability of the ternary fission in isotopes of element with $Z = 126$ compared to actinides, suggesting its potential observability as a stability test for the superheavy elements. Additionally, investigations into the ^{298}114 nucleus show nearly equal fission barriers for the binary and the ternary fission within 10%, which emphasizes the competition between them [24]. Analysis of the results obtained for the kinetic energy of fission fragments in the ternary fission of even-even isotopes, based on the Q-values produced in the reaction, provides insights into the fission exit channels for its different geometries [25]. Recent studies have increased our understanding of the dynamics of the ternary fission. Subramanian et al. [26] analyzed the mass distribution of fission fragments in the ternary fission of superheavy nuclei, revealing the dominance of asymmetric fragmentation at certain excitation energies and showing that the shell effects play a prominent role in this case. Mahesh Babu et al. [27] identified minimal driving potentials and high penetration probabilities for the LCP-accompanied ternary fission configurations involving closed shell magic isotopes. Sowmya et al. [28] compared the α-decays, the binary fission, and the ternary fission in ^{281}Ds superheavy isotope, emphasizing the dominance of the α-decays due to their shorter half-lives and higher probabilities.

This study builds upon our earlier work on the equatorial geometry of the ternary fission for ^{248}Cf [29], where we investigated the emission of the LCPs such as ^{4}He, ^{10}Be, ^{14}C, ^{14}N, and ^{16}O. Here, we extend our analysis to explore broader aspects of true ternary fission dynamics, focusing on theoretical interpretations and configurations involving heavy and superheavy isotopes.

I. THEORETICAL METHODS OF CALCULATIONS

A. Kinetic energy distribution

In ternary fission, the energy released (Q-value) is determined based on the Three Cluster Model TCM using the following relation:

$$Q = M_x - \sum_{i=1}^{3} m_{i,x}, \tag{1}$$

Here, M stands for the mass excess of the parent nuclei, and m_i (for $i = 1, 2, 3$) represent the mass excess of three product fragments, measured in MeV units [30]. For the ternary fission to occur, the energy produced in the reaction must be a positive value, which appears as the kinetic energy of the three fragments in the exit channel.

The kinetic energy of the fragments are calculated based on the momentum and energy conservation principles in a sequential collinear decay process. This involves two steps as indicated in Figure 1. The initial breakup of the parent nucleus and the subsequent breakup of the intermediate composite fragment have been shown in this figure [31].

Direct decomposition into three parts (democratic decay), similar to other ternary decay processes, occupies a much smaller phase space compared to successive binary decays. As a result, sequential binary decays dominate the triple fission mechanism. For the collinear cluster tripartition (CCT), the sequential model is employed to determine the velocities as well as the kinetic energies of fragments in the collinear geometry, under the assumption of spherical shapes for simplicity at this stage.

Step I:

$$A \rightarrow A_i + A_{jk}. \tag{2}$$

Step II:

$$A \rightarrow A_i + (A_{jk} \rightarrow A_j + A_k), \tag{3}$$

Therefore, the results of two steps is

$$A \rightarrow A_i + A_j + A_k. \tag{4}$$

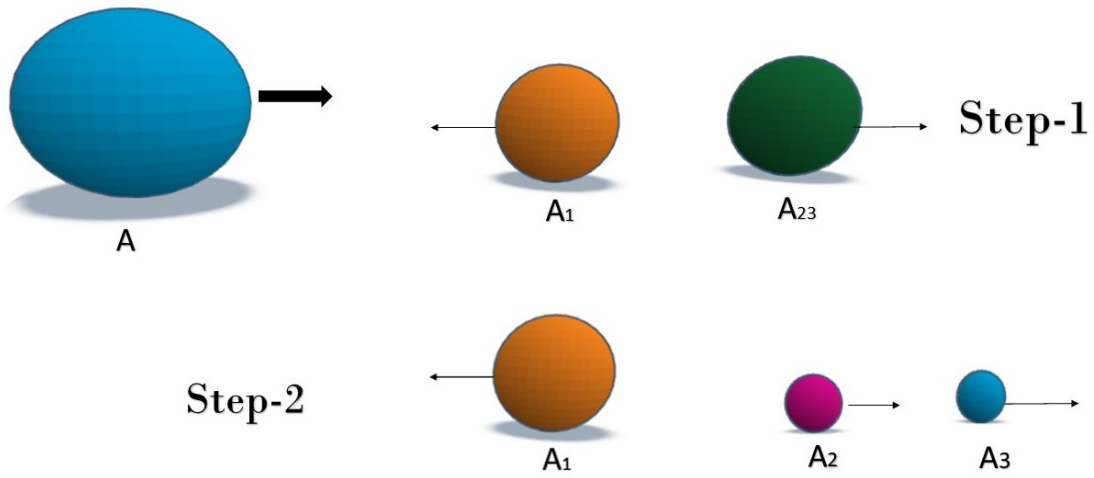

FIG. 1: A scheme for the ternary breakup of a parent nucleus into three fragments in the collinear geometry, which is a two steps process.

For the ternary decay process, the Q-value is expressed as:

$$Q = M_x - \sum_{i=1}^{3} m_{i,x}, \tag{5}$$

where the symbols retain their aforementioned meanings.

In this framework, the Q-value for the first fragmentation step, wherein the parent nucleus A disintegrates into A_i and A_{jk}, is given by:

$$Q_I = M_x(A) - [m_x(A_i) + m_x(A_{jk})]. \tag{6}$$

In the second step, where the composite fragment, A_{jk} breaks into A_j and A_k, the interaction Q-value is obtained using

$$Q_{II} = m_x(A_{jk}) - [m_x(A_j) + m_x(A_k)]. \tag{7}$$

Assuming energy and momentum conservation principles, the effective Q-value, Q_I^{eff} represents the energy shared as the kinetic energies of A_i and A_{jk}

$$Q_I^{\text{eff}} = Q_I + E_A^* - E_{A_i}^* - E_{A_{jk}}^*, \tag{8}$$

where E^*_A, $E^*_{A_i}$, and $E^*_{A_{jk}}$ denote the excitation energies of the parent nucleus A and the fragments A_i and A_{jk}, respectively.

By applying the momentum conservation principle in the center-of-mass (c.m.) frame for Step I one obtain

$$P_{A_i} + P_{A_{jk}} = 0, \tag{9}$$

or equivalently,

$$m_{A_i} v_{A_i} + m_{A_{jk}} v_{A_{jk}} = 0, \tag{10}$$

where m_{A_i} and $m_{A_{jk}}$ represent the masses, and v_{A_i} and $v_{A_{jk}}$ are the velocities of A_i and A_{jk}, respectively.

The energy conservation equation for Step I is

$$Q_I + E^*_A = \frac{1}{2} m_{A_i} v^2_{A_i} + E^*_{A_i} + \frac{1}{2} m_{A_{jk}} v^2_{A_{jk}} + E^*_{A_{jk}}, \tag{11}$$

which simply rewritten as

$$Q^{\text{eff}}_I = \frac{1}{2} m_{A_i} v^2_{A_i} + \frac{1}{2} m_{A_{jk}} v^2_{A_{jk}}. \tag{12}$$

Solving these equations yields the velocities:

$$v_{A_{jk}} = \sqrt{\frac{2m_{A_i}}{m_{A_i} + m_{A_{jk}}} \frac{Q^{\text{eff}}_I}{m_{A_{jk}}}}, \tag{13}$$

$$v_{A_i} = -\sqrt{\frac{2m_{A_{jk}}}{m_{A_i} + m_{A_{jk}}} \frac{Q^{\text{eff}}_I}{m_{A_i}}}. \tag{14}$$

From the velocities, the kinetic energies are obtained

$$E_{A_{jk}} = \frac{m_{A_i}}{m_{A_i} + m_{A_{jk}}} Q^{\text{eff}}_I, \tag{15}$$

$$E_{A_i} = \frac{m_{A_{jk}}}{m_{A_i} + m_{A_{jk}}} Q^{\text{eff}}_I. \tag{16}$$

For Step II, where A_{jk} splits into A_j and A_k, the momentum conservation principle gives

$$m_{A_{jk}} v_{A_{jk}} = m_{A_j} v_{A_j} + m_{A_k} v_{A_k}, \tag{17}$$

with v_{A_j} and v_{A_k} being the velocities of fragments with A_j and A_k mass numbers, and m_{A_j} and m_{A_k} are their respective masses. The energy conservation equation gives

$$Q_{II} + \frac{1}{2} m_{A_{jk}} v_{A_{jk}}^2 + E^*_{A_{jk}} = \frac{1}{2} m_{A_j} v_{A_j}^2 + E^*_{A_j} + \frac{1}{2} m_{A_k} v_{A_k}^2 + E^*_{A_k}. \tag{18}$$

On the left-hand side of this equation, we include not only the Q-value, Q_{II}, but also the excitation energy $E^*_{A_{jk}}$ of the composite fragment A_{jk}, along with its kinetic energy. This total energy on the left side is distributed as the excitation and kinetic energies of the fragments A_j and A_k. As in step I, by shifting all the excitation energies to the left-hand side, we arrive at

$$Q_{II\text{eff}} + \frac{1}{2} m_{A_{jk}} v_{A_{jk}}^2 = \frac{1}{2} m_{A_j} v_{A_j}^2 + \frac{1}{2} m_{A_k} v_{A_k}^2, \tag{19}$$

where

$$Q_{II\text{eff}} = Q_{II} + E^*_{A_{jk}} - E^*_{A_j} - E^*_{A_k}. \tag{20}$$

To simplify the analysis, we initially assume that all excitation energies are negligible, approximating a scenario akin to cold fragmentation, specifically for the chosen decay case involving spherical fragments. This leads to the following energy conservation equation:

$$Q_{II} + \frac{1}{2} m_{A_{jk}} v_{A_{jk}}^2 = \frac{1}{2} m_{A_j} v_{A_j}^2 + \frac{1}{2} m_{A_k} v_{A_k}^2. \tag{21}$$

The velocity of the fragment A_k is determined by solving Eqs. (15) and (19) as:

$$v_{A_k} = \frac{m_{A_k} m_{A_{jk}} v_{A_{jk}} \pm \sqrt{\xi^2}}{m_{A_k}^2 + m_{A_j} m_{A_k}}, \tag{22}$$

where

$$\xi^2 = m_{A_k}^2 m_{A_{jk}}^2 v_{A_{jk}}^2 - \Big[(m_{A_k}^2 + m_{A_j} m_{A_k}) \times (m_{A_{jk}}^2 v_{A_{jk}}^2) - 2 m_{A_j} Q_{II} - m_{A_j} m_{A_{jk}} v_{A_{jk}}^2 \Big]. \tag{23}$$

Since Eq. (20) arises from solving a quadratic equation, there are two potential velocity solutions. Using Eq. (20), the kinetic energy of fragment A_k is given by:

$$E_{A_k} = \frac{1}{2} m_{A_k} v_{A_k}^2. \tag{24}$$

The velocity of fragment A_j, denoted as v_{A_j}, is derived by substituting v_{A_k} from Eq. (20) into Eq. (15):

$$v_{A_j} = -\left[\frac{m_{A_k} v_{A_k} - m_{A_{jk}} v_{A_{jk}}}{m_{A_j}}\right]. \tag{25}$$

Subsequently, the kinetic energy of fragment A_j is computed as follows:

$$E_{A_j} = \frac{1}{2} m_{A_j} v_{A_j}^2. \tag{26}$$

Thus, the kinetic energies of all three fragments are determined.

B. Calculation of ternary fission half-life

The ternary fission is fundamentally similar to binary fission, although in the ternary fission, LCPs are emitted in the final scission stage. Exploring the kinematics and dynamics of the ternary fission enriches our understanding of the fission process and the nuclear structure. Several theoretical frameworks have been formulated to study the trajectories of LCPs emitted during fission. These frameworks are very important in investigating the static and dynamic properties of the fissioning nucleus, the scission configuration, and the overall dynamics of the fission process [32, 33].

The TCM describes the cold spontaneous ternary fission by incorporating interaction potentials among the fission fragments, such as the Coulomb, the nuclear, and the centrifugal potentials [**?**]. The repulsive Coulomb forces act to separate the fragments, while nuclear forces provide an attractive counterbalance. For even-even isotopes undergoing cold ternary fission, production of even-even fragments dominate over even-odd and odd-odd fragments, allowing the centrifugal term to be disregarded. The resulting interaction potential between fragment pairs is expressed as:

$$V = \sum_{i=1}^{3} \sum_{j>i} (V_c^{ij} + V_p^{ij}), \tag{27}$$

where V_{ij}^c and V_{ij}^p denote the Coulomb and the nuclear interaction potentials between fragments i and j, respectively. The Coulomb interaction potential for the spherical fragments defined as follows

$$V_c^{ij} = \frac{Z_i Z_j e^2}{R_{ij}}. \tag{28}$$

furthermore, Z_i and Z_j are the atomic numbers of the fragments, and R_{ij} is the center-to-center distance between fragments i and j. The effective radius R_x for a fragment is calculated using the following semi-empirical relation [34]

$$R_x = 1.28A_x^{\frac{1}{3}} - 0.76 + 0.8A_x^{-\frac{1}{3}}. \tag{29}$$

The nuclear proximity potential $V_p(s)$, essential for describing the interaction of a pair of fragments, is expressed as follows [35]

$$V_p(s) = 4\pi\gamma R_\delta \Phi\left(\frac{s}{b}\right), \tag{30}$$

where $\Phi(\xi)$, a universal function dependent on the reduced separation distance $\xi = s/b$, is defined as [36]:

$$\Phi(\xi) = \begin{cases} -\frac{1}{2}(\xi - 2.54)^2 - 0.0852(\xi - 2.54)^3, & \text{if } \xi < 1.2511, \\ -3.437\exp(-\xi/0.75), & \text{if } \xi \geq 1.2511. \end{cases} \tag{31}$$

The geometry of the fragments plays a crucial role in determining quantities such as penetration probability, decay constant, yield, and half-life in the ternary fission. Two main configurations—the collinear and the equatorial—are commonly used in the ternary fission. In the collinear arrangement, the fragments align along a single straight line, while in the equatorial geometry, the LCP is emitted perpendicularly to the separation line of the other fragments. These geometries significantly influence energy distribution, and angular momentum of fragments. Figure 2 illustrates these geometries for fragments separation configuration ($s > 0$).

In equatorial geometry, symmetric separation of the fragments is assumed, with identical distances and velocities ($s = s_{12} = s_{13} = s_{23}$). However, due to the Coulomb repulsion often speed of fragments are not identical, most pronounced in the lightest fragment (A_3, or LCP). To account for this, the relation $k \times s_{12} = s_{13} = s_{23}$ is introduced, where k ranges $0 < k < 1$ [37–39]. Despite these variations, relative yields and potential barriers remain largely unaffected by k, justifying the assumption $k = 1$. In the collinear geometry, where A_3 occupies the central position, the surface distance between fragments is given as:

$$s = s_{13} = s_{23}, \tag{32}$$

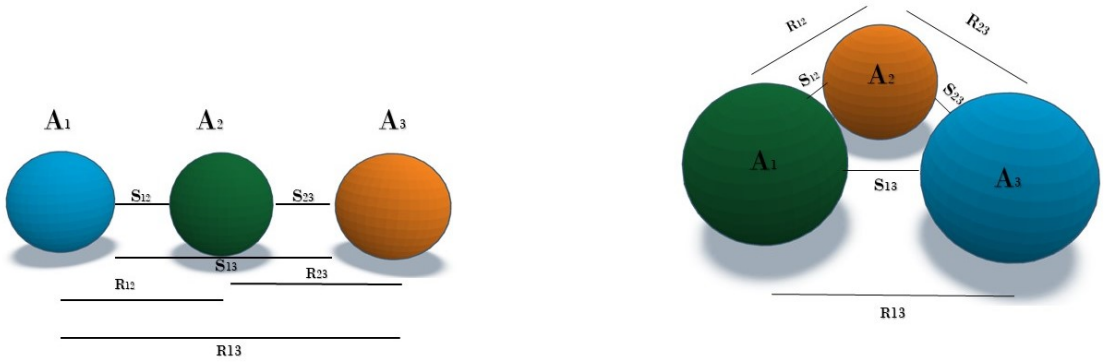

FIG. 2: Schematic of the ternary fission geometries for separated fragments $s > 0$: (Left) The equatorial, and (Right) The collinear geometry.

and the center-to-center distance between the outer fragments is expressed as:

$$s_{12} = 2(R_3 + s). \tag{33}$$

The nuclear surface tension coefficient γ, which is used in these calculations, is determined using Lysenkov's semi-empirical formula [40]:

$$\gamma = 0.9517 \left[1 - \frac{1.7826(N-Z)^2}{A^2}\right] \quad \left(\frac{\text{MeV}}{\text{fm}}\right)^2. \tag{34}$$

The relative yield $Y(A_i, Z_i)$ for a specific fragment combination in the TCM framework is given by:

$$Y(A_i, Z_i) = \frac{P(A_i, Z_i)}{\sum P(A_i, Z_i)}, \tag{35}$$

where $P(A_i, Z_i)$, the penetration probability for a specific pathway, is calculated using the Wentzel-Kramers-Brillouin (WKB) approximation:

$$P = \exp\left(-\frac{2}{\hbar}\int_{S_{\text{in}}}^{S_{\text{out}}} \sqrt{2\mu(V-Q)}\, dS\right). \tag{36}$$

Here, S_{in} and S_{out} are the inner and outer turning points, respectively. The reduced mass μ of the system is evaluated as follows

$$\mu = m\left(\frac{A_1A_2A_3}{A_1A_2 + A_1A_3 + A_2A_3}\right), \tag{37}$$

where m denotes the average mass of nucleon. The half-life for a given combination i is then calculated as:

$$T_{\frac{1}{2}}^{i} = \frac{\ln 2}{\lambda_i} = \frac{\ln 2}{\nu_i P_i}. \tag{38}$$

II. RESULTS AND DISCUSSION

In this study, we analyzed the ternary fission of ^{254}Cf, focusing on fragment combinations and their properties across the collinear and the equatorial geometries. The study also includes an analysis of 40 of the most favored combinations of 128 unique Z_1, Z_2, Z_3 groups selected from over 45,000 possible combinations with positive Q-values. The atomic numbers of selected combinations ranged from $Z = 20$ to $Z = 52$. These combinations are detailed in Table I. Since the analysis examines configurations where A_1, A_2, or A_3 occupies the middle position, there is no distinction between equivalent permutations of Z_1, Z_2, Z_3 (e.g., Z_1, Z_2, Z_3 is equivalent to Z_2, Z_1, Z_3, and so on). The table summarizes the calculated Q-values, driving potentials $(V_e, V_{A3}, V_{A2}, V_{A1})$, penetration probabilities $(P_e, P_{A3}, P_{A2}, P_{A1})$, decay constants $(\lambda_e, \lambda_{A3}, \lambda_{A2}, \lambda_{A1})$, and assault frequency (ν) for these combinations.

A notable aspect of this study is the calculation of the fragments energy distribution, which are summarized in Table II. Additionally, Figures 5a, 5b, and 5c illustrate the kinetic energy distributions for the first, second, and third fragments, respectively. This energy analysis provides critical insights into the dynamics of the ternary fission process.

For the collinear geometry, the driving potential (V) was systematically examined for each fragments configuration, where each of fragments A_1, A_2, or A_3 occupies the middle position. The relationship between the Q-value and the atomic numbers Z_1, Z_2, and Z_3 is depicted in Figure 3. Among the analyzed configurations, ^{82}Ge +^{84} Ge +^{88} Se exhibits the highest Q-value of 268.78 MeV. This combination, with $A_3 =^{84}$ Ge in the middle, has the lowest driving potential of 22.18 MeV (Figure 4c) and a penetration probability of 2.01×10^{-25}. The nuclear structure of this fragments combination is noteworthy: ^{82}Ge and ^{88}Se are both even-even nuclei with magic and even neutron numbers ($N = 50$ and $N = 54$), while ^{84}Ge is near-magic ($N = 52$). These structural attributes enhance the stability of the configuration, reducing the driving potential and increasing the probability of fission.

When A_1 occupies the middle position, the driving potential decreases significantly due to

the reduced Coulomb interactions between the heavier fragments at the ends. For instance, in the combination ^{50}Ca+^{72}Ni+^{132}Sn, the driving potential is only 0.04 MeV (Figure 4a) with the highest penetration probability of all combinations about, 1.39×10^{-13}. Here, ^{132}Sn, a double-magic nucleus ($Z = 50, N = 82$), plays a pivotal role in stabilizing the configuration. ^{72}Ni and ^{50}Ca, while not double-magic, are even-even and near-magic, further contributing to the favorable characteristics of this fragmentation.

Similarly, placing A_2 in the middle leads to moderate driving potentials, balancing the effects of the Coulomb repulsion and the nuclear stabilization. For ^{50}Ca $+^{72}$ Ni $+^{132}$ Sn, with $A_2 =^{72}$ Ni in the middle, the driving potential is 13.29 MeV (Figure 4b) with a penetration probability of 5.25×10^{-20}. This is higher than when the lightest fragment A_1 occupies the middle position but remains the highest penetration probability for A_2 in the middle. This configuration benefits from the double-magic nature of ^{132}Sn and the magic structure of ^{50}Ca, emphasizing the significant influence of fragments structural properties on driving potential and fission probabilities.

In equatorial geometry, the driving potential is consistently higher, and penetration probabilities are significantly lower due to the increased Coulomb repulsion among symmetrically placed fragments. For the combination ^{50}Ca $+^{72}$ Ni $+^{132}$ Sn in equatorial geometry, the driving potential rises to 83.84 MeV (Figure 4d), while the decay constants calculated for this configuration reinforce these findings, with $\lambda_{cA1} = 9.46 \times 10^{8}$, $\lambda_{cA2} = 3.58 \times 10^{2}$, and $\lambda_{\text{equ}} = 4.01 \times 10^{-27}$. These values confirm that collinear geometries, particularly with A_1 or A_2 in the middle, are more conducive to the ternary fission.

The analysis of kinetic energy distributions provides additional evidence for the impact of fragment configuration on fission dynamics. For the first fragment, the combination ^{76}Ni $+^{86}$ Se $+^{92}$ Kr exhibits the highest kinetic energy, with $K_1 = 201.70$ MeV, $K_2 = 30.17$ MeV, and $K_3 = 30.93$ MeV (Figure 5a). For the second fragment, combination ^{82}Ge $+^{84}$ Ge $+^{88}$ Se achieves the highest average kinetic energy of 89.59 MeV, with $K_1 = 174.98$ MeV, $K_2 = 49.10$ MeV, and $K_3 = 44.69$ MeV (Figure 5b). Finally, for the third fragment, fragmentation ^{82}Ge $+^{85}$ As $+^{87}$ As demonstrates the highest kinetic energy, with $K_1 = 171.03$ MeV, $K_2 = 44.14$ MeV, and $K_3 = 50.15$ MeV (Figure 5c).

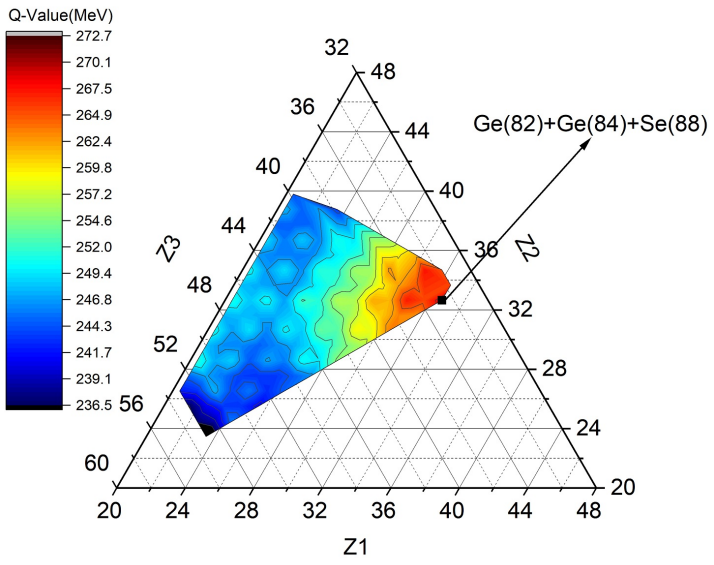

FIG. 3: Q-Value as a function of the atomic numbers of fragments Z_1, Z_2, and Z_3 in the collinear geometry.

III. CONCLUSIONS

In this study, we explored the impact of fragment geometry and the nuclear structure on the stability and the dynamics of the ternary fission of the ^{254}Cf isotope. The findings underscore the critical influence of fragment arrangement and the nuclear structure on fission characteristics, with a focus on the distinctions between the collinear and the equatorial geometries in the ternary fission of the ^{254}Cf isotope.

The placement of fragments plays a pivotal role in shaping the driving potential and the overall stability of each combination. When the heaviest fragment, A_3, is positioned centrally, the configuration achieves maximum stability, as evidenced by its significantly long half-life of 3.38×10^2 seconds, as detailed in Table III. This stability arises from the reduced Coulomb repulsion and the effective distribution of energy among the fragments, consistent with the findings reported in Ref. [41].

Conversely, placing the lightest fragment, A_1, at the center yields the least stable configuration, characterized by the shortest half-life of 7.19×10^{-10} seconds. This geometry reduces the driving potential due to the decreased Coulomb interaction among fragments pair, resulting in higher penetration probability and facilitating the fission process. This behavior is particularly notable in the collinear geometries, where the lightest fragment in

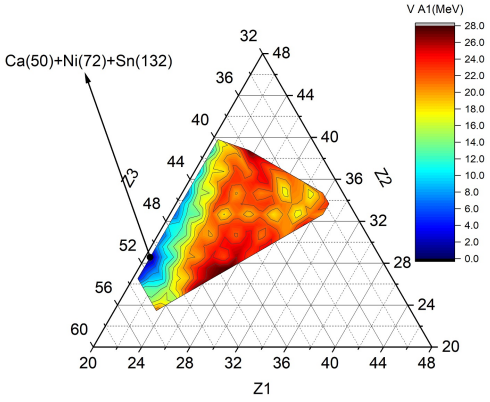

(a) Case I: The collinear geometry with A_1 in the middle.

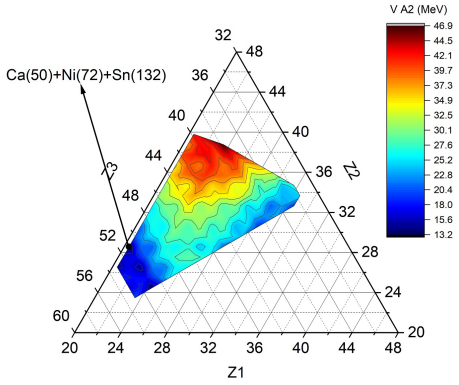

(b) Case II: The collinear geometry with A_2 in the middle.

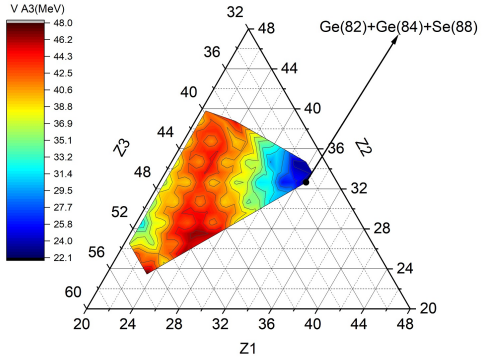

(c) Case III: The collinear geometry with A_3 in the middle.

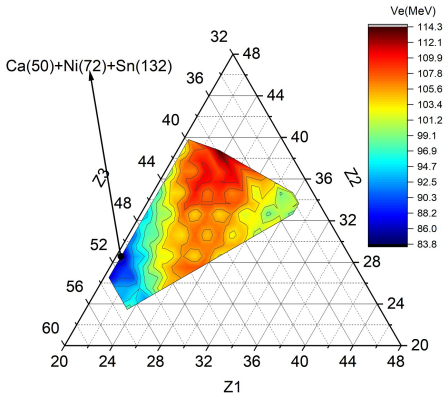

(d) Case IV: The equatorial geometry.

FIG. 4: Driving potential as a function of atomic numbers Z_1, Z_2, and Z_3 for various cases and combinations of the ternary fission for ^{254}Cf isotope.

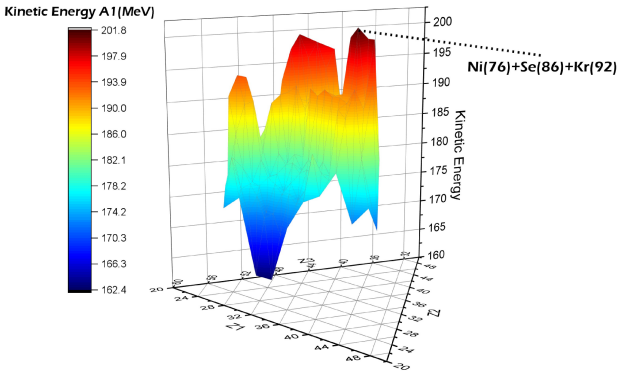

(a) Case I: Distribution of the kinetic energy of fragment A_1.

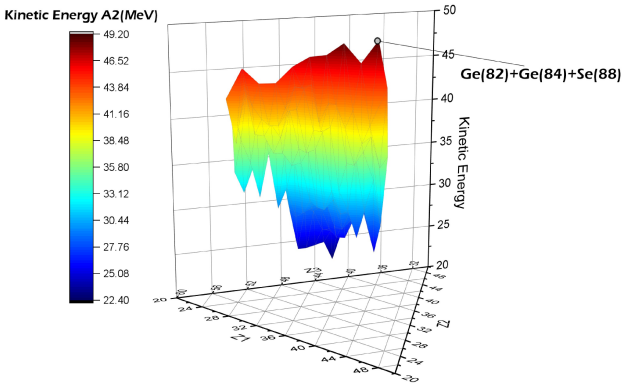

(b) Case II: Distribution of the kinetic energy of fragment A_2.

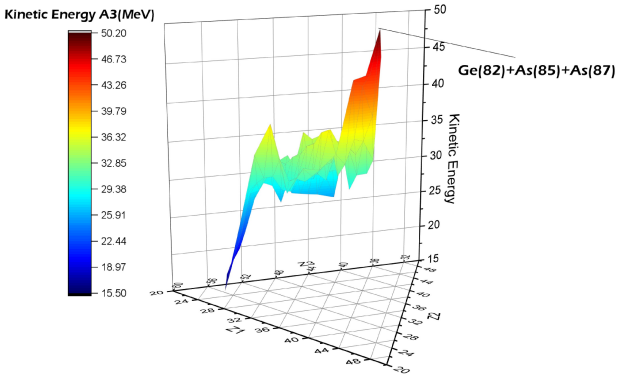

(c) Case III: Distribution of the kinetic energy of fragment A_3.

FIG. 5: Distribution of the kinetic energy shared among three fragments in the collinear geometry of the ternary fission for ^{254}Cf isotope.

the middle exhibits the lowest driving potential and the highest penetration probability, making it the most favorable combination.

Intermediate stability is observed when the fragment A_2 is centrally located, with a calculated half-life of 1.46×10^{-2} seconds. These configurations effectively balance the driving potential and the energy distribution among fragments, offering a compromise between the extreme cases.

The equatorial geometries exhibit the highest stability overall, with a remarkable calculated half-life of 1.72×10^{26} seconds. This extraordinary stability is attributed to the symmetric energy distribution and minimized driving potential inherent in the equatorial fragments combinations.

An important insight into ternary fission processes is the minimal kinetic energy absorption by the centrally positioned light fragment in the collinear fragmentation. The majority of the kinetic energy is transferred to the other two fragments, potentially explaining the frequent experimental non-detection of the third fragment. This observation aligns with the findings reported in Ref. [31]. Kinetic energy distributions for fragment combinations depicted in Fig. 5a and the corresponding Q-values and the total kinetic energies listed in Table II reveal a consistent pattern. The near-identical values across different combinations highlight the cold nature of the ternary fission, with minimal heat dissipation and uniform energy partitioning.

In conclusion, our analysis reveals that collinear geometries are generally more favorable for the true ternary fission when fragment placements optimize stability and kinetic energy distribution. These findings contribute to a deeper understanding of the ternary fission mechanisms, emphasizing the importance of structural configurations in predicting fission dynamics and stability.

TABLE I: Calculated values for different geometries of the ternary fission of ^{254}Cf isotope. The Q-value and driving potentials (V_e, V_{A3}, V_{A2}, V_{A1}) are in MeV. Penetrating probabilities (P_e, P_{A3}, P_{A2}, P_{A1}) and decay constants (λ_e, λ_{A3}, λ_{A2}, λ_{A1}) are dimensionless. Values of ν are scaled by $\times 10^{21}$.

Combination	**Q**	$\mathbf{V}_e$	$\mathbf{V}_{A3}$	$\mathbf{V}_{A2}$	$\mathbf{V}_{A1}$	$\mathbf{P}_e$	$\mathbf{P}_{A3}$	$\mathbf{P}_{A2}$	$\mathbf{P}_{A1}$	ν	$\lambda_\mathbf{e}$	$\lambda_{\mathbf{A3}}$	$\lambda_{\mathbf{A2}}$	$\lambda_{\mathbf{A1}}$
^{82}Ge+^{84}Ge+^{88}Se	268.79	22.18	19.17	20.05	98.01	1.28e-57	2.01e-25	5.04e-24	2.53e-24	7.28	9.3e-36	1.8e-02	3.7e-02	1.5e-03
^{80}Zn+^{86}Se+^{88}Se	267.38	23.23	24.04	16.88	98.78	3.12e-58	5.22e-26	2.80e-26	4.88e-23	7.24	2.3e-36	3.5e-01	2.0e-04	3.8e-04
^{80}Zn+^{82}Ge+^{92}Kr	267.17	25.78	20.98	16.76	98.43	4.95e-58	3.59e-27	7.74e-25	5.67e-23	7.24	3.6e-36	4.1e-01	5.6e-03	2.6e-05
^{82}Ge+^{85}As+^{87}As	265.56	23.62	24.46	23.37	101.40	8.04e-60	2.34e-26	1.22e-26	4.52e-26	7.19	5.8e-38	3.3e-04	8.8e-05	1.7e-04
^{81}Ga+^{82}Ge+^{91}Br	265.49	26.24	23.12	21.06	100.90	1.58e-59	1.49e-27	6.19e-26	5.04e-25	7.19	1.1e-37	3.6e-03	4.5e-04	1.1e-05
^{80}Zn+^{85}As+^{89}Br	264.45	27.83	25.02	19.71	101.55	4.31e-60	2.69e-28	5.52e-27	1.49e-24	7.16	3.1e-38	1.1e-02	3.9e-05	1.9e-06
^{78}Zn+^{80}Zn+^{96}Sr	263.39	30.89	19.55	20.49	100.48	1.43e-59	8.81e-30	1.78e-24	8.49e-25	7.13	1.0e-37	6.1e-03	1.3e-02	6.3e-08
^{80}Zn+^{81}Ga+^{93}Rb	263.24	30.83	22.42	20.25	101.59	2.86e-60	8.87e-30	7.95e-26	7.23e-25	7.13	2.0e-38	5.2e-03	5.7e-04	6.3e-08
^{79}Ga+^{81}Ga+^{94}Kr	262.87	29.52	23.41	24.32	103.03	6.19e-61	2.85e-29	3.04e-26	1.50e-26	7.12	4.4e-39	1.1e-04	2.2e-04	2.0e-07
^{76}Ni+^{86}Se+^{92}Kr	262.80	29.43	27.57	16.72	101.53	2.80e-60	3.49e-29	3.35e-28	3.31e-23	7.12	2.0e-38	2.4e-01	2.4e-06	2.5e-07
^{79}Cu+^{87}Br+^{88}Se	261.53	28.64	31.18	19.99	103.84	8.97e-62	5.86e-29	5.37e-30	6.12e-25	7.08	6.3e-40	4.3e-03	3.8e-08	4.1e-07
^{50}Ca+^{72}Ni+^{132}Sn	251.70	30.93	13.29	0.05	83.85	5.88e-49	1.74e-28	5.25e-20	1.39e-13	6.82	4.0e-27	9.5e+08	3.6e+02	1.2e-06
^{60}Cr+^{62}Cr+^{132}Sn	245.65	38.28	13.73	14.88	92.39	1.05e-54	6.76e-33	1.01e-20	3.78e-21	6.65	7.0e-33	2.5e+01	6.7e+01	4.5e-11
^{54}Ti+^{68}Fe+^{132}Sn	247.53	36.18	14.69	9.78	90.05	6.50e-53	1.63e-31	4.41e-21	2.85e-18	6.70	4.4e-31	1.9e+04	3.0e+01	1.1e-09
^{52}Ca+^{68}Fe+^{134}Te	242.04	36.77	14.79	3.92	86.33	5.53e-52	3.41e-32	1.61e-21	4.70e-16	6.55	3.6e-30	3.1e+06	1.1e+01	2.2e-10
^{56}Ti+^{64}Cr+^{134}Te	236.94	42.62	16.44	14.36	92.82	2.61e-56	1.11e-35	1.02e-22	2.16e-21	6.42	1.7e-34	1.4e+01	6.5e-01	7.1e-14
^{52}Ca+^{69}Co+^{133}Sb	244.92	35.84	16.50	3.21	87.04	7.67e-52	1.64e-31	4.73e-22	1.49e-15	6.63	5.1e-30	9.9e+06	3.1e+00	1.1e-09
^{53}Sc+^{68}Fe+^{133}Sb	242.93	38.48	16.68	8.85	90.20	1.02e-53	5.96e-33	2.56e-22	3.69e-18	6.58	6.7e-32	2.4e+04	1.7e+00	3.9e-11
^{53}Sc+^{69}Co+^{132}Sn	247.04	36.13	17.10	6.84	89.56	1.01e-52	1.69e-31	3.66e-22	5.53e-17	6.69	6.8e-31	3.7e+05	2.4e+00	1.1e-09
^{57}V+^{65}Mn+^{132}Sn	243.29	40.60	17.59	15.71	94.66	4.24e-56	3.83e-34	1.01e-22	1.62e-21	6.59	2.8e-34	1.1e+01	6.6e-01	2.5e-12
^{56}Ti+^{65}Mn+^{133}Sb	240.66	41.04	17.73	13.02	93.06	9.36e-56	1.44e-34	5.46e-23	1.83e-20	6.52	6.1e-34	1.2e+02	3.6e-01	9.4e-13
^{59}V+^{62}Cr+^{133}Sb	238.73	43.12	18.25	16.68	95.27	2.51e-57	7.46e-36	2.49e-23	1.71e-22	6.47	1.6e-35	1.1e+00	1.6e-01	4.8e-14
^{53}Sc+^{67}Mn+^{134}Te	236.22	43.14	18.58	13.28	93.14	2.38e-56	7.71e-36	9.79e-24	1.13e-20	6.40	1.5e-34	7.2e+01	6.3e-02	4.9e-14
^{59}V+^{61}V+^{134}Te	231.66	47.93	20.11	21.27	98.19	3.81e-60	5.67e-39	8.83e-25	3.54e-25	6.27	2.4e-38	2.2e-03	5.5e-03	3.5e-17
^{48}Ca+^{75}Cu+^{131}In	248.06	36.25	20.37	7.29	90.91	2.21e-52	5.71e-31	2.81e-23	1.70e-16	6.72	1.5e-30	1.1e+06	1.9e-01	3.8e-09
^{48}Ca+^{78}Zn+^{128}Cd	250.29	35.23	20.78	6.44	90.92	2.70e-52	1.93e-30	1.72e-23	4.17e-16	6.78	1.8e-30	2.8e+06	1.2e-01	1.3e-08
^{54}Ti+^{72}Ni+^{128}Cd	248.55	38.08	20.99	12.31	94.88	2.08e-55	1.59e-32	4.76e-24	1.77e-19	6.73	1.4e-33	1.2e+03	3.2e-02	1.1e-10
^{53}Sc+^{70}Ni+^{131}In	247.35	37.31	21.04	8.47	92.43	4.85e-54	4.68e-32	7.37e-24	1.15e-17	6.70	3.2e-32	7.7e+04	4.9e-02	3.1e-10
^{50}Ca+^{82}Ge+^{122}Pd	250.96	35.99	25.24	6.24	93.50	2.31e-54	2.84e-31	6.11e-26	1.75e-16	6.80	1.6e-32	1.2e+06	4.2e-04	1.9e-09
^{52}Ca+^{86}Se+^{116}Ru	250.18	37.42	30.28	6.94	96.59	7.25e-57	1.72e-32	9.09e-29	2.58e-17	6.78	4.9e-35	1.7e+05	6.2e-07	1.2e-10
^{52}Ca+^{83}As+^{119}Rh	248.10	39.14	30.59	8.26	97.42	1.91e-57	2.07e-33	6.33e-29	5.93e-18	6.72	1.3e-35	4.0e+04	4.3e-07	1.4e-11
^{52}Ca+^{92}Kr+^{110}Mo	248.91	38.81	34.52	9.32	99.68	6.98e-59	2.33e-33	4.34e-31	1.47e-18	6.74	4.7e-37	9.9e+03	2.9e-09	1.6e-11
^{48}Ca+^{81}Ga+^{125}Ag	247.71	38.80	25.80	10.25	95.50	4.05e-55	1.98e-32	4.39e-26	5.34e-18	6.71	2.7e-33	3.6e+04	2.9e-04	1.3e-10
^{72}Ni+^{74}Ni+^{108}Mo	255.02	38.40	21.90	22.91	103.04	1.60e-61	8.89e-34	1.21e-25	5.51e-26	6.91	1.1e-39	3.8e-04	8.3e-04	6.1e-12
^{74}Ni+^{82}Ge+^{98}Sr	261.88	31.46	25.01	18.12	101.52	3.61e-60	3.64e-30	6.22e-27	1.09e-23	7.09	2.6e-38	7.7e-02	4.4e-05	2.6e-08
^{71}Co+^{83}As+^{100}Sr	255.20	37.16	33.31	23.10	107.63	3.04e-64	2.09e-33	3.65e-31	2.89e-26	6.91	2.1e-42	2.0e-04	2.5e-09	1.4e-11
^{57}V+^{82}Ge+^{115}Tc	246.99	43.74	34.67	21.72	107.11	2.91e-63	3.20e-36	2.39e-31	1.28e-24	6.69	1.9e-41	8.6e-03	1.6e-09	2.1e-14
^{52}Ca+^{89}Br+^{113}Tc	246.69	41.07	35.35	11.05	101.10	7.11e-60	1.33e-34	1.50e-31	1.89e-19	6.68	4.7e-38	1.3e+03	1.0e-09	8.9e-13
^{68}Fe+^{83}As+^{103}Y	253.36	38.87	34.24	22.59	107.87	2.15e-64	2.94e-34	1.37e-31	6.19e-26	6.86	1.5e-42	4.3e-04	9.4e-10	2.0e-12
^{52}Ca+^{98}Sr+^{104}Zr	247.75	39.32	37.89	11.03	101.75	2.91e-60	1.02e-33	5.97e-33	1.81e-19	6.71	1.9e-38	1.2e+03	4.0e-11	6.9e-12

TABLE II: Total Q-value and distribution of the kinetic energies shared among fragments in true ternary fission of ^{254}Cf isotope for the various combinations in the collinear geometry.

A1	**K(MeV)**	**A2**	**K(MeV)**	**A3**	**K(MeV)**	**Q(MeV)**
^{82}Ge	174.99	^{84}Ge	49.11	^{88}Se	44.70	268.79
^{80}Zn	193.15	^{86}Se	35.29	^{88}Se	38.94	267.38
^{80}Zn	192.92	^{82}Ge	38.06	^{92}Kr	36.20	267.17
^{82}Ge	171.27	^{85}As	44.14	^{87}As	50.15	265.56
^{81}Ga	182.41	^{82}Ge	40.13	^{91}Br	42.96	265.49
^{80}Zn	189.86	^{85}As	38.74	^{89}Br	35.85	264.45
^{78}Zn	180.22	^{80}Zn	48.68	^{96}Sr	34.48	263.39
^{80}Zn	188.49	^{81}Ga	41.67	^{93}Rb	33.07	263.24
^{79}Ga	172.29	^{81}Ga	46.70	^{94}Kr	43.87	262.87
^{76}Ni	201.70	^{86}Se	30.17	^{92}Kr	30.93	262.80
^{79}Cu	199.97	^{87}Br	28.54	^{88}Se	33.01	261.53
^{50}Ca	193.21	^{72}Ni	34.24	^{132}Sn	24.25	251.70
^{60}Cr	175.52	^{62}Cr	45.73	^{132}Sn	24.40	245.65
^{54}Ti	179.40	^{68}Fe	43.30	^{132}Sn	24.83	247.53
^{52}Ca	190.43	^{68}Fe	33.69	^{134}Te	17.92	242.04
^{56}Ti	176.91	^{64}Cr	42.65	^{134}Te	17.38	236.94
^{52}Ca	193.61	^{69}Co	31.31	^{133}Sb	19.99	244.92
^{53}Sc	184.65	^{68}Fe	37.45	^{133}Sb	20.83	242.93
^{53}Sc	189.24	^{69}Co	34.86	^{132}Sn	22.94	247.04
^{57}V	176.54	^{65}Mn	43.48	^{132}Sn	23.27	243.29
^{56}Ti	181.10	^{65}Mn	39.20	^{133}Sb	20.35	240.66
^{59}V	181.68	^{62}Cr	37.59	^{133}Sb	19.46	238.73
^{53}Sc	177.09	^{67}Mn	42.03	^{134}Te	17.10	236.22
^{59}V	173.70	^{61}V	42.44	^{134}Te	15.52	231.66
^{48}Ca	182.26	^{75}Cu	36.54	^{131}In	29.26	248.06
^{48}Ca	184.77	^{78}Zn	35.32	^{128}Cd	30.20	250.29
^{54}Ti	180.55	^{72}Ni	37.64	^{128}Cd	30.36	248.55
^{53}Sc	189.58	^{70}Ni	30.88	^{131}In	26.88	247.35
^{50}Ca	192.39	^{82}Ge	29.11	^{122}Pd	29.47	250.96
^{52}Ca	199.40	^{86}Se	24.17	^{116}Ru	26.60	250.18
^{52}Ca	197.12	^{83}As	24.17	^{119}Rh	26.81	248.10
^{52}Ca	198.01	^{92}Kr	24.64	^{110}Mo	26.26	248.91
^{48}Ca	181.87	^{81}Ga	34.78	^{125}Ag	31.07	247.71
^{72}Ni	175.39	^{74}Ni	47.16	^{108}Mo	32.46	255.02
^{74}Ni	191.24	^{82}Ge	35.59	^{98}Sr	35.05	261.88
^{71}Co	190.07	^{83}As	30.09	^{100}Sr	35.04	255.20
^{57}V	180.73	^{82}Ge	30.50	^{115}Tc	35.76	246.99
^{52}Ca	195.57	^{89}Br	24.50	^{113}Tc	26.63	246.69
^{68}Fe	188.71	^{83}As	29.50	^{103}Y	35.16	253.36
^{52}Ca	196.73	^{98}Sr	25.37	^{104}Zr	25.64	247.75

TABLE III: Calculated half-lives (in seconds) for different geometries of the ternary fission for ^{254}Cf isotope.

Geometry	**Half-life (seconds)**
The equatorial	1.72×10^{26}
The collinear with fragment A_1 located in the middle	7.19×10^{-10}
The collinear with fragment A_2 located in the middle	1.46×10^{-2}
The collinear with fragment A_3 located in the middle	3.38×10^{2}

[1] L Meitner, O Hahn and F Strassmann, *Z. Phys*, **106**, 249 (1937).

[2] M. R. Pahlavani and M. Joharifard, "Ternary fission studies of ^{252}Cf with various cluster emissions", *Eur. Phys. J. A*, **54**, 171 (2018). DOI: 10.1140/epja/i2018-12602-7.

[3] M. R. Pahlavani and M. Joharifard, "Investigation of cluster formation in ternary fission of ^{252}Cf using different Skyrme interactions", *Phys. Rev. C*, **99**, 044601 (2019). DOI: 10.1103/PhysRevC.99.044601.

[4] M. R. Pahlavani and S. M. Mirfathi, "Investigation of potential energy surfaces in ternary fission of ^{252}Cf", *Phys. Rev. C*, **93**, 044617 (2016). DOI: 10.1103/PhysRevC.93.044617.

[5] M. R. Pahlavani and S. M. Mirfathi, "Study of the influence of fragment mass and charge on ternary fission characteristics of ^{252}Cf", *Phys. Rev. C*, **92**, 024622 (2015). DOI: 10.1103/PhysRevC.92.024622.

[6] M. R. Pahlavani and D. Naderi, "Study of cluster emission in the ternary fission of ^{252}Cf using realistic potentials", *Eur. Phys. J. A*, **48**, 129 (2012). DOI: 10.1140/epja/i2012-12129-y.

[7] M. R. Pahlavani and D. Naderi, "Analysis of the role of cluster configurations in ternary fission of ^{252}Cf", *Phys. Rev. C*, **83**, 024602 (2011). DOI: 10.1103/PhysRevC.83.024602.

[8] M. R. Pahlavani and P. Mehdiour, "Investigation of fragment yields in the ternary fission of ^{252}Cf using the Skyrme energy density formalism", *Int. J. Mod. Phys. E*, **27**(3), 1850018 (2018). DOI: 10.1142/S0218301318500180.

[9] M. R. Pahlavani and P. Mehdiour, "Study of the effect of nuclear structure on the ternary fission of ^{252}Cf", *Nucl. Sci. Tech.*, **29**, 146 (2018). DOI: 10.1007/s41365-018-0482-1.

[10] M. R. Pahlavani and S. M. Mirfathi, "Microscopic study of ternary fission of ^{252}Cf with emission of ^{4}He, ^{10}Be, and ^{14}C clusters", *Phys. Rev. C*, **96**, 014606 (2017). DOI: 10.1103/PhysRevC.96.014606.

[11] L. Rosen and A. M. Hudson, "Theory of cluster decay in fission", *Phys. Rev.*, **78**, 533 (1950). DOI: 10.1103/PhysRev.78.533.

[12] Z.Ren, D. Vertenar, T.Niksic, P. W. Zhao, J. Zhao, and J. Meng, "Dynamical synthesis of ^{4}He in the scission phase of nuclear fission", *Phys. Rev. Lett.*, **128**, 172501 (2022). DOI: .

[13] F. Fossati and T. Pinelli, "Geometrical and dynamical state of the ^{252}Cf nucleus at the scission point as determined from the experimental results of ternary fission", *Nucl. Phys. A*, **244**, 243

(1975). DOI: 10.1016/0375-9474(75)90100-1.

[14] W. von Oertzen and A. K. Nasirov, "The role of the cluster structure in fission and fusion reactions", *Phys. Lett. B*, **734**, 234 (2014). DOI: 10.1016/j.physletb.2014.05.067.

[15] San-Tsiang, Chastel, H. O. Zah-Wei, L. Vigneron, and R. Chastel, "Study of nuclear reactions and fission processes", *C. R. Acad. Sci. (Paris)*, **223**, 986 (1946). DOI: 10.1051/jphysrad:01948009010600.

[16] T. San-Tsiang, H. O. Zah-Wei, L. Vigneron, and R. Chastel, "Research on ternary fission", *C. R. Acad. Sci. (Paris)*, **224**, 272 (1947). DOI: 10.1016/S0577-9073(24)00114-X.

[17] T. San-Tsiang, H. O. Zah-Wei, L. Vigneron, and R. Chastel, "On the fission processes in heavy nuclei", *Phys. Rev.*, **71**, 382 (1947). DOI: 10.1103/PhysRev.71.382.2.

[18] T. San-Tsiang, H. O. Zah-Wei, R. Chastel, and L. Vigneron, "Study of the fission process in heavy elements", *J. Phys. Radium*, **8**, 165 (1947). DOI: 10.1051/jphysrad:0194700806016500.

[19] T. San-Tsiang, H. O. Zah-Wei, L. Vigneron, et al., "Fission of heavy nuclei", *Nature*, **159**, 773 (1947). DOI: 10.1038/159773a0.

[20] E. W. Titterton and T. A. Brinkley, "On the binary and ternary photofission of thorium-232", *The London, Edinburgh, and Dublin Philosophical Magazine and Journal of Science*, **41**(316), 500-503 (1950). DOI: 10.1080/14786445008561436.

[21] K. F. Flynn, L. E. Glendenin, and E. P. Steinberg, "Search for Be^{10} as a product of ternary fission", *Phys. Rev.*, **101**(5), 1492 (1956). DOI: 10.1103/PhysRev.101.1492.

[22] P. O. Hess, S. Misicu, W. Greiner, and W. Scheid, "Collective modes of tri-nuclear molecules", *J. Phys. G: Nucl. Part. Phys.* **26**, 957 (2000). DOI: 10.1088/0954-3899/26/6/315.

[23] H. Schultheis and R. Schultheis, "Prediction of ternary fission rates for element 126", *Phys. Rev. C*, **15**, 1601(R) (1977). DOI: 10.1103/PhysRevC.15.1601.

[24] H. Schultheis and R. Schultheis, "Ternary fission and the stability of superheavy elements", *Phys. Lett. B*, **50**, 322 (1974). DOI: 10.1016/0370-2693(74)90624-8.

[25] D. N. Poenaru, W. Greiner, and R. A. Gherghescu, "Energy released in ternary fission", *At. data Nucl. data Tab.*, **68**, 147 (1998). DOI: 10.1006/adnd.1997.0758.

[26] S. Subramanian, M. T. Senthil Kannan, S. Selvaraj, "Ternary Fission Mass Distributions of Superheavy Nuclei Within a Statistical Model", *Braz. J. Phys.*, **51**, 136 (2021). DOI: 10.1007/s13538-020-00264-9.

[27] A. V. Mahesh Babu, N. Sowmya, H. C. Manjunatha, N. Dhananjaya, "A Study on Light

Charged Particle Accompanied Ternary Fission of 253Cf", *Phys. Scr.*, **2023**, 100185 (2023). DOI: 10.1016/j.physo.2023.100185.

[28] N. Sowmya, H. C. Manjunatha, N. Dhananjaya, A. M. Nagaraja, "Competition Between Binary Fission, Ternary Fission, Cluster Radioactivity and Alpha Decay of 281Ds", *J. Radioanal. Nucl. Chem.*, **323**, 1347–1351 (2020). DOI: 10.1007/s10967-019-06846-9.

[29] M. R. Pahlavani and M. Saeidi Babi, "Study of the ^{4}He, ^{10}Be, ^{14}C, ^{14}N, and ^{16}O accompanied ternary fission of ^{248}Cf isotope in the fragments equatorial geometry", *Chin. J. Phys.*, **89**, 469 (2024). DOI: 10.1016/j.cjph.2024.03.025.

[30] M. Wang, W. J. Huang, F. G. Kondev, G. Audi, and S. Naimi, "The AME2020 atomic mass evaluation: (II) tables, graphs, and references", *Chin. Phys. C*, **45**, 030003 (2021). DOI: 10.1088/1674-1137/abddaf.

[31] K. R. Vijayaraghavan, W. von Oertzen, and M. Balasubramaniam, "Kinetic energies of cluster fragments in ternary fission of ^{252}Cf", *Eur. Phys. J. A*, **48**, 27 (2012). DOI: 10.1140/epja/i2012-12027-4.

[32] F. Fossati and T. Pinelli, "On the fusion-fission dynamics and the emission of intermediate mass fragments", *Nucl. Phys. A*, **249**, 185-204 (1975). DOI: 10.1016/0375-9474(75)90100-1.

[33] A. K. Sinha and G. K. Mehta, "Mass distributions of fission fragments for actinide nuclei", *Phys. Rev. C*, **21**, 2467 (1980). DOI: 10.1103/PhysRevC.21.2467.

[34] J. Blocki, J. Randrup, W. J. Swiatecki, and C. F. Tsang, "Nuclear fission: The process and its applications", *Ann. Phys.*, **105**(2), 427 (1977). DOI: 10.1016/0003-4916(77)90249-4.

[35] K. R. Vijayaraghavan, M. Balasubramaniam, and W. von Oertzen, "Study of ternary fission in heavy nuclei", *Phys. Rev. C*, **90**, 024601 (2014). DOI: 10.1103/PhysRevC.90.024601.

[36] J. Blocki and W. J. Swiatecki, "Nuclear fission and the deformation of fissioning nuclei", *Ann. Phys. (NY)*, **132**, 53 (1983). DOI: 10.1016/0003-4916(81)90268-2.

[37] K. Manimaran and M. Balasubramaniam, "Investigation of the ternary fission of actinide nuclei", *Eur. Phys. J. A*, **45**, 293 (2010). DOI: 10.1140/epja/i2010-11000-7.

[38] K. Manimaran and M. Balasubramaniam, "Investigation of ternary fission of actinide nuclei", *Phys. Rev. C*, **83**, 034609 (2011). DOI: 10.1103/PhysRevC.83.034609.

[39] K. Manimaran and M. Balasubramaniam, "Ternary fission of actinide nuclei", *J. Phys. G*, **37**, 045104 (2010). DOI: 10.1088/0954-3899/37/4/045104..

[40] K. P. Santhosh and S. Krishnan, "Ternary fission of actinide nuclei", *Eur. Phys. J. A*, **52**, 108

(2016). DOI: 10.1140/epja/i2016-16108-0.

[41] A. V. Karpov, "Ternary fission in actinide nuclei", *Phys. Rev. C*, **94**, 064615 (2016). DOI: 10.1103/PhysRevC.94.064615.